Benchmarking water adsorption on metal surfaces with ab-initio molecular dynamics

Mianle Xu,[1] Sihang Liu,[1] Sudarshan Vijay,[1] Thomas Bligaard,[1] and Georg Kastlunger[1, a)]

Catalysis Theory Center, Department of Physics, Technical University of Denmark, Denmark

Solid-water interfaces are ubiquitous in nature and technology. Particularly, in technologies evolving in the context of a green transition, such as electrochemistry, the junction of an electrolyte and an electrode is a central part of the device. Simulations based on density functional theory (DFT) have become de facto standard for both the understanding of atomistic processes at this interface and the screening for new materials. Thus, DFT's ability to simulate the solid/water interaction needs to be benchmarked and ideal simulation setups need to be identified, in order to prevent systematic errors. Here, we developed a rigorous sampling protocol for benchmarking the adsorption/desorption strength of water on metallic surfaces against experimental temperature programmed desorption, single crystal adsorption calorimetry and thermal energy atom scattering. We screened DFT's quality on a series of transition metal surfaces, applying three of the most common exchange correlation approximations; PBE-D3, RPBE-D3 and BEEF-vdW. We find that all three XC-functional reflect the pseudo-zeroth order desorption of water rooted in the combination of attractive adsorbate-adsorbate interactions at low coverages and their saturation at intermediate coverage. However, both RPBE-D3 and BEEF-vdW lead to more appropriate water binding strengths, while PBE-D3 clearly overbinds near-surface water. We are able to relate the variations in binding strength to specific variations in water-metal and water-water interactions, highlighting the structural consequences inherent in an uninformed choice of simulation parameters. Our study gives atomistic insight into the complex adsorption equilibrium of water and represents a guideline for future DFT-based simulations of the solvated solid interface within molecular dynamics studies by providing an assessment of systematic errors in specific setups.

[a)]Electronic mail: geokast@dtu.dk

I. INTRODUCTION

Water-Metal interfaces play a vital role in many physical and chemical process, for example, heterogeneous and electro-catalysis, batteries and corrosion[1,2]. The atomistic understanding of such interfaces has improved substantially in recent decades[3,4], particularly for electrochemical interfaces[5], water structure/clusters/network at the surface[6,7] and multilayer growth of water at metal surface[8]. Given the vast amount of past (and certainly upcoming) research efforts on understanding this interface, the intersection of a solid and liquid phase is heavy in demand regarding the quality of the theoretical methodologies,[9,10] which were predominantly optimized for the respective separated phases. However, significant strides have been made in theoretical modeling in recent decades. Density functional theory (DFT)-based calculations have been remarkably successful in calculating surface adsorption energies of various molecules, thus allowing the prediction of reaction networks within heterogeneous catalysis.[11] Further, first-principles calculations were able to give atomistic insights to the phase diagram of monolayer, nanoconfined water[7].

Steadily increasing computational capabilities have made ab initio molecular dynamics (AIMD) a viable approach for simulating solid-water interfaces[12–15], today. On their basis, the revised Perdew-Burke-Enzerhof exchange-correlation (XC) functional (RPBE)[16], with semi-empirical dispersion corrections (D3), has been shown to provide a more accurate description of water-water and water-metal interactions than its original formulation, PBE[17–22]. Despite these advancements, accurately capturing water behavior at interfaces remains a significant challenge[23]. Theoretical considerations and atomic-scale simulations are subjects of ongoing critical debate[9].

Notably, there is a paucity of accurate AIMD simulations benchmarked against experimental results on water adsorption/desorption processes. Arguably, the most fundamental phenomenon inherent to the water-metal interface is the low-dimensional adsorption of water on the solid surface at ultra-high vacuum (UHV) conditions. Although comprising only a fraction of the complexity of a real solid-liquid interface, it is this aspect that allows an accurate assessment of water's adsorption strength in experiments, by studying thermally activated desorption[24,25], as well as atomistic simulations.

Among the rigorous experimental methods for studying the water adsorption strength on well-defined single crystal surfaces, Temperature-Programmed Desorption (TPD) is most

prominent[26]. Interpreting TPD results for extracting adsorption strengths has recently gained interest, as a means for benchmarking theoretically predicted adsorption properties.[27] Here, some of us have recently developed a model allowing the definition of adsorption energy and adsorbate-adsorbate interaction parameters directly from experimental spectra,[28] which will form the basis of our benchmark against this experimental technique.

Besides TPD, thermal energy atom scattering (TEAS), often referred to specular He scattering, is a molecular beam technique that allows the detection of vibrational dynamics and adsorption characteristics on surfaces[29]. TEAS has previously been applied for studying the adsorption, desorption, and clustering behavior of H_2O on Pt(111)[25]. Finally, single crystal adsorption calorimetry (SCAC)[30], is able to estimate the heat of H_2O adsorption/desorption directly at single crystal metal surfaces at varying coverages.

In this paper, we present an AIMD-DFT benchmark for water adsorption at varying water-metal interfaces against experimental results from TPD, TEAS and SCAC. Our test set comprised the (111)-facets of Au, Cu, Pt and Ni, as well as the (211)-step of Pt covered in a variety of low-dimensional water-films. The PBE-D3, RPBE-D3 and BEEF-vdW XC-functionals, have been compared regarding their reliability and performance. The results showed that the water binding strength is functional-dependent following the order of BEEF-vdW < RPBE-D3 < PBE-D3, where both BEEF-vdW and RPBE-D3 do predict the metal-water interaction in good agreement with the experimental data, while PBE-D3 tends to overbind. We further find that the differences in water-metal interactions lead to distinct near-surface water densities among the of the varying XC-functionals, while the water-water interaction is only marginally affected by their variation. The fundamental groundwork conducted in our benchmark will enable future studies of solvated interfaces to circumvent systematic errors and, thereby building a foundation for a more detailed atomistic understanding of water's unique interaction with solid surfaces.

II. METHODS

A. Computational Details

All DFT calculations in this paper have been performed with the Vienna Ab Initio Simulation Package(VASP)[31], employing the projector-augmented wave(PAW) method[32] in com-

bination with a plane wave basis set in periodic boundary condition. Plane wave cutoff energies of 500eV, together with a Gaussian smearing with a width of 0.1eV were chosen. SCF-convergence was set to a total energy difference of less than 10^{-4} eV. D_2O was simulated instead of H_2O in the AIMD, applying a timestep of 1 femto seconda (1 fs) within a NVT ensemble at 140K set by a Nose-Hoover thermostat.

The metal surfaces, constructed applying the Atomic Simulation Environment(ASE)[33], were chosen as 3x4 supercells for Pt(111),Au(111),Cu(111),Ni(111) facets and with a 1x4 supercell (12 surface atoms) for Pt(211). Four layers of metal were used perpendicular to the surface with the bottom two being constrained to their respective bulk structure. A 4x3x1 Γ-point centered Monkhorst-Pack k-point grid was applied to sample the Brillouin zone[34]. A dipole correction was applied perpendicular to the slab surface.

In our benchmark, we combined three XC functionals within the generalized gradient approximation (GGA) level with added dispersion corrections, namely the Perdew-Burke-Ernzerhof functional[22] with Grimme D3[35] correction (PBE-D3), the revised Perdew-Burke-Ernzerhof functional[16] with Grimme D3 correction (RPBE-D3) and the Bayesian error estimation functional[36] including van der Waals interactions(BEEF-vdW)[37]. The lattice constants of Au, Pt, Ni and Cu metals obtained for the employed PBE-D3,RPBE-D3 and BEEF-vdW scheme based on 1x1x1 bulk unit cell and a k-point density consistent 11x11x11 k-point grid are tabulated in the Supplemental Data.

Zero point energy(ZPE) and vibrational frequencies were computed for each functional separately within a harmonic approximation (IBRION=5), where 30 configurations were sampled from the equilibrium region in AIMD region. The results of quantities are tabulated in Table III in supplementary information and The sampling are discussed in Section X of the Supplementary information.

B. Benchmark workflow

Figure 1 shows a flowchart of the benchmark procedure applied in this paper. Our method consists of three main processes: The first consists of conducting AIMD simulations at varying (thin-film) coverages of water on a series of metal surfaces. This stage involves a reasonable selection strategy of the AIMD's initial structures and appropriate statistics for estimating the convergence of the AIMD results as will be described in Section II C

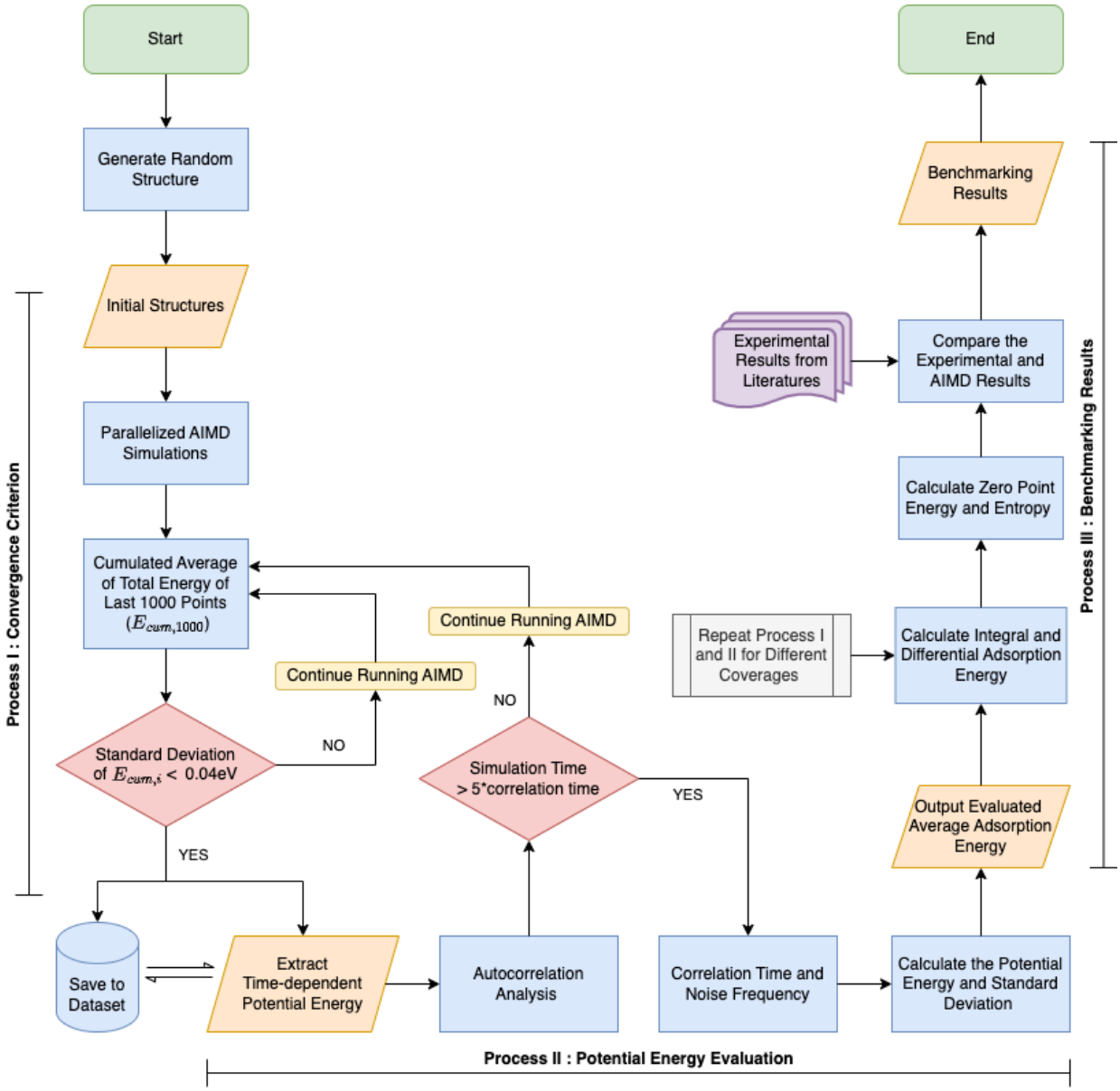

Figure 1. Flowchart of our benchmarking procedure

and in more detail in Section 1 of the SI. The second stage of our analysis is the potential energy evaluation after achieving AIMD convergence. As we will describe in detail in Section II D, we analyzed several energetic quantities, finally leading to the differential adsorption/desorption energies applied in the comparison with experiments. The third process consists of retrieving the relevant adsorption/desorption energetics from experimental data, described in section II E and the definition of the most appropriate thermodynamic quantities, as well as assumptions for the benchmark, as we will describe in detail in Section II F.

C. AIMD Statistics

The water/metal surfaces are modeled with water coverages up to one water molecule per metal surface atom, resulting from 1 to 12 water molecules and coverages of $\theta = \frac{n}{12}$ (n=1,2,3,...,12). All the selected initial structures, the related AIMD running results are given in Figure S14-S19.

A series of water coverages were modeled starting from randomized initial structures with the strategy varying on the specific metals and facets. In the case of water on Au(111), Pt(111) and Cu(111) surfaces, we ran AIMD on 30-50 randomly created initial trajectories at the coverages of 0.75 monolayers (ML) for Au and Pt, and 1ML on Cu. Two lowest energy trajectories were chosen for a first covergence of the AIMD trajectory. Initial guesses for the trajectories at other coverages were then created by adding or deleting single water molecules out of this most stable trajectory.

In conctrast to Au, Pt and Cu, in the case of Ni(111), we started from 15 random initial trajectories for both spin resolved and unresolved Ni(111) surfaces at each studied coverage. Finally, on stepped Pt(211), four different initial trajectories ate each coverage were applied to run the AIMD until convergence was achieved, two of which were random initial guesses, the other two consisted of the extreme cases of all hydrogens pointing away from and towards the surface, respectively, as illustrated in Figure S5. Further details are given in Section I of supplementary information.

Each of the MD trajectories was run between 3ps to 30ps, varying with the size of the simulated system and the quality of the initial guesses. Convergence of individual trajectories was assumed if the standard deviation of the cumulative average of the total energy ($E_{cum,i}$) reduced below 0.04eV within the last 1ps. $\overline{E}_{cum,i}$ was defined as

$$\overline{E}_{cum,i} = \overline{E}_{cum,i-n} + \frac{1}{n}(E_i - E_{i-n}), \tag{1}$$

where E_i refers to the total energy (kinetic + potential energy) of image, i and n means the number of steps after equilibration (i>n).

The applied convergence criterion was defined as

$$Standard\ Deviation(SD) = \sqrt{\frac{1}{N}\sum_{i=1}^{N}(\overline{E}_{cum,i} - \overline{E}_{cum,1ps})^2} < 0.04eV \tag{2}$$

where N=1000 is the number of steps in the previous 1ps and $\overline{E}_{cum,1ps}$ is the cumulative

total energy of the last 1000 steps. The value of 0.04eV was chosen to limit the uncertainty to less than 10% of the actual adsorption energies, which range at ≈0.5eV.

The average potential energy ($\overline{E}$) has been calculated as the average within the equilibrated time frame of the AIMD, following

$$\overline{E} = \frac{1}{N}\sum_{i=1}^{N}(E_i) \tag{3}$$

.

Both fluctuations around a mean value and some correlation between different pieces, originating from the Nose-Hoover thermostat and the dynamic nature of water at the interface have been estimated by applying the autocorrelation function(ACF)[38] for time lag i,

$$\gamma_i = \frac{\sum_{j=1}^{N-i-1}((E_j - \overline{E})(E_{i+j} - \overline{E}))}{\sum_{i=1}^{N}(E_i - \overline{E})^2}, \tag{4}$$

where the correlation time is

$$\tau = \sum_{i=1}^{N}\gamma_i \tag{5}$$

The AIMD running time scale should be much longer than τ, where we chose the criterion of that the AIMD runtime scale should exceed 5 times of τ. τ is also roughly the estimation of the pre-equilibrium time period.

In the Figure 1, we present a flowchart summarizing the complete workflow within our benchmark study.

D. Calculation of water adsorption energies

We define the average adsorption (potential) energy $\Delta E_{avg}(\theta)$ as

$$\Delta E_{avg}(\theta) = \frac{\overline{E}_{Slab+N_{ads}\cdot H_2O} - \overline{E}_{Slab} - N_{ads}\cdot E_{H_2O(g)}}{N_{ads}}, \qquad \theta = \frac{N_{ads}}{N_{sites}}, \tag{6}$$

with $\overline{E}_{Slab+N\cdot H_2O}$ being the energy of the metal with number of N_{ads} water molecules at the surface resulting, $\overline{E}_{Slab}$ the energy of the bare metal slab (both resulting from our AIMD trajectories), $E_{H_2O(g)}$ the energy of water molecule in gas phase, N_{ads} the number of water molecule(s) on the slab surface and N_{sites} as the number of surface atoms. We sample 12

different coverage structures ($N_{ads} = 1, 2, 3, ..., 12$) and through these AIMD datasets, the differential adsorption energy can be calculated from the average adsorption energy, as

$$\Delta E_{dif}(\theta) = \frac{d(N_{ads} \cdot \Delta E_{avg})}{dN_{ads}} = \frac{d(\theta \cdot \Delta E_{avg})}{d\theta} = \frac{d(\Delta E_{int})}{d\theta} \tag{7}$$

also giving access to the integral adsorption energy,

$$\Delta E_{int}(\theta) = \theta \cdot \Delta E_{avg}(\theta) \tag{8}$$

From the AIMD results, we firstly calculate the average adsorption energy $\overline{E}$ vs. coverage. To obtain the differential adsorption energy, we apply the linear fitting over integral adsorption energy and coverage, where the slope is ΔE_{dif}.

E. Interpretation of experimental results

From the experimental research, the desorption of monolayer water has been identified to follow (Pseudo-)zeroth order kinetics. Thus, the central fitting equation applied to the TPD spectra is an Arrhenius type equation of the form $r_{des} = A(T)exp(-\frac{\Delta G^{\ddagger}_{des}}{k_{\mathrm{B}}T})$, where r_{des} is the desorption rate (ML/s), $A(T)$ is the pre-exponential factor, $\Delta G^{\ddagger}_{des}$ is the activation free energy of desorption, k_{B} is the Boltzmann constant, T is the temperature. The desorption energy can simply be obtained from a linear fit of $ln(r_{des})$ against $1/T$, where the slope is $-\Delta G^{\ddagger}_{des}/k_{\mathrm{B}}$, by assuming $A(T)$ is slowly varying. From TEAS, by analysing the specular helium intensity in different isothermal conditions, an Arrhenius plot of the desorption rate vs. $1/T$ was sampled, where the kinetic parameter $\Delta G^{\ddagger}_{des}$ could be obtained[25]. In SCAC, the calorimetry directly provided ΔH_{ads}, which was adopted from[39,40].

F. Thermodynamic assumptions within benchmark

To analyse the adsorption/desorption energy from the experimental desorption kinetics, we will apply several thermodynamic assumptions, as outlined in figure 2: (i) the change in entropy for the (adsorbed) initial state to the transition state is negligible. (ii) the potential energy of the transition state is well approximated by the energy of the final state. (iii) the adsorption and desorption processes are reversible, which allows us to calculate the desorption energy based on adsorption energies of water.

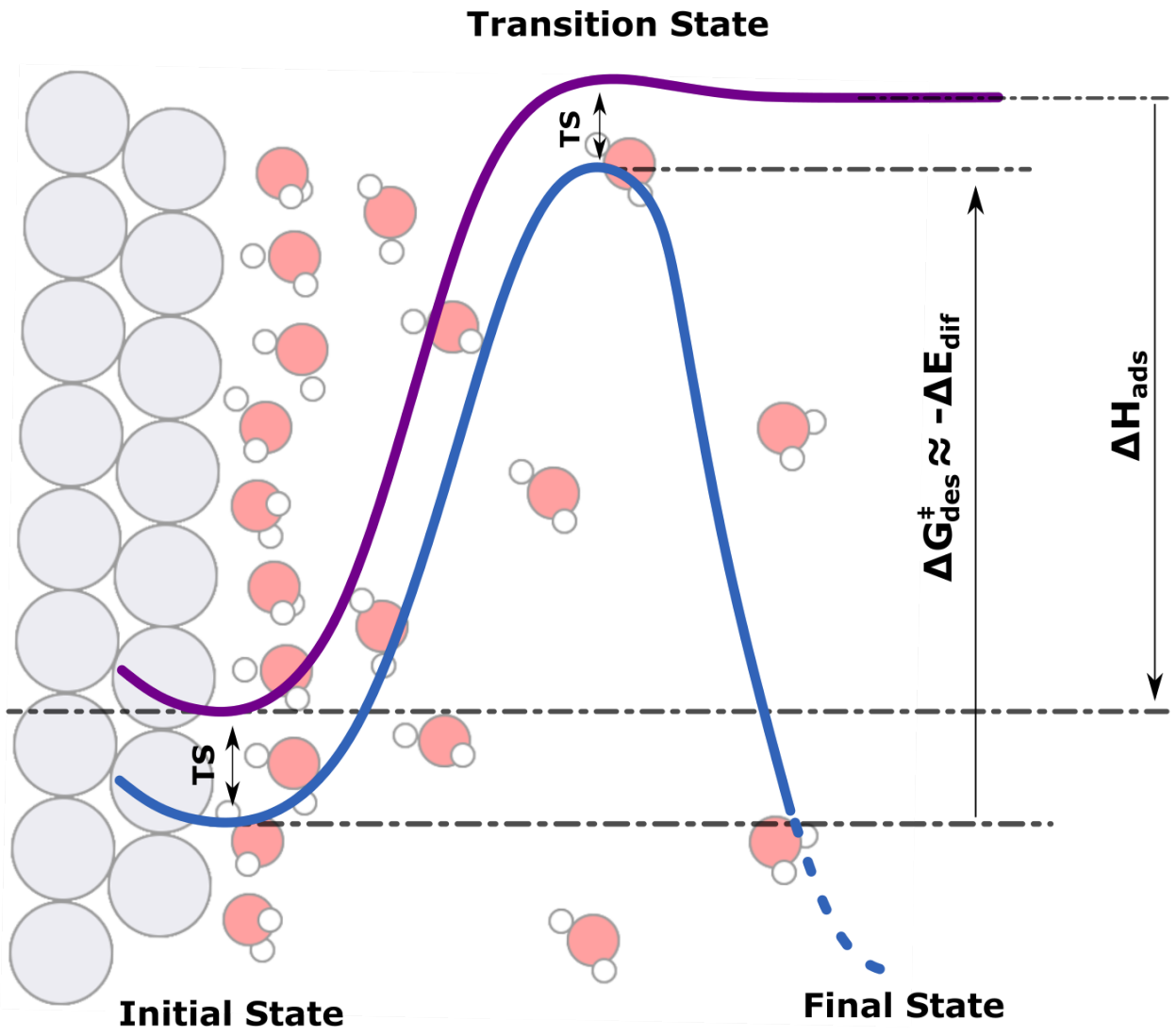

Figure 2. Schematic outlining the applied assumption that the activation free energy of water desorption can be approximated by the differential desorption energy. The blue and purple lines represent the free energy and heat of desorption, respectively, where the latter is used within our benchmark.

Applying approximations (i)-(iii) allows us to equate the free activation energy of desorption in experiments with potential energies of adsorption obtained from our AIMD simulations and simplifies the thermodynamics at the hearth of the benchmark into,

$$\Delta G^{\ddagger}_{des} \approx -\Delta E_{dif}, \tag{9}$$

where ΔE_{dif} is the differential adsorption energy calculated by AIMD, allowing a straight-

forward benchmark against TPD and TEAS experiments. On the other hand,

$$\Delta H_{ads} = \Delta E_{dif} + \Delta ZPE + \int_0^T C_p dT, \tag{10}$$

with ΔZPE as the difference of zero point energy between initial state and final state of the reaction and C_p being the constant-pressure heat capacity, allows a validation against SCAC experiments.

III. RESULTS AND DISCUSSION

A. Water adsorption energetics

We start our assessment with the discussion of water adsorption on the fcc(111) metal surfaces of Pt, Au, Cu, and Ni. The respective ΔE_{avg} and ΔE_{int} at varying θs are shown in Figure 3 a-h. Two general features are obtained from analyzing ΔE_{avg} vs. θ: First, at low coverage ΔE_{avg} decreases with increasing coverage, suggesting an attractive adsorbate-adsorbate interaction, rooted in the formation of a hydrogen bond network. Secondly, this attractive interaction saturates between 0.5-0.75ML, where the exact saturation coverage varies among the studies metal surfaces.

The functional shape of ΔE_{avg} vs. θ can be explained based on the classification of water adsorption by dividing it into different categories depending on the behavior of the first water layer[41]. At low coverage, water molecules mostly interact with the metal surface, while the water-water interaction build up gradually upon increasing the coverage, between 0.5-0.75ML a first complete water layer is formed. Beyond this coverage, the water-water interaction dominates the water adsorption energy, since the wetting from water molecules in the first layer prevents the interaction between the newly added water molecules and metal surface. We will further discuss the details of this effect once we will analyze the spatial water distribution on the metal surface.

From the average adsorption energies in Figure 3 a,c and e, we are able to calculate the integral adsorption energies, based on the equation 8. The results shown in Figure 3 b,d,f and h for Pt(111),Au(111),Cu(111) and Ni(111) respectively. To calculate ΔE_{dif}, we fitted the integral adsorption energies linearly and the slopes are tabulated inside the respective panels of figure 3. The good linear fit, with all R^2-values being tabulated in Table II in supplementary information, justifies a zeroth-order interpretation for desorption from our

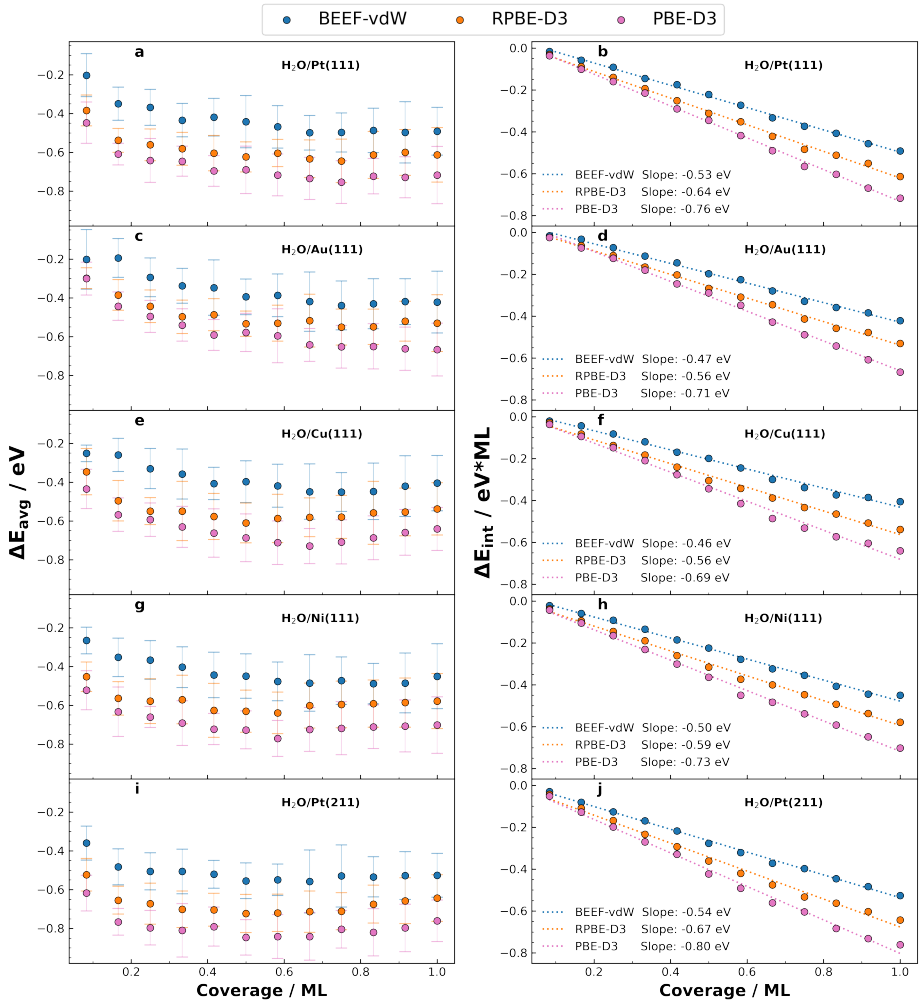

Figure 3. Water adsorption energies on varying metal surfaces and applying 3 different XC-functionals as a function of water coverage. The left and right panels show the average adsorption energies,$\Delta E_{avg}(\theta)$, and the integral adsorption energies, $\Delta E_{int}(\theta)$, repsectively, while the rows refer to the varying metal surfaces. The slopes resulting from a linear regression of $\Delta E_{int}(\theta)$, representing ΔE_{dif}, are given inside the right-hand panels. All the data in this figure represent the trajectory of lowest energy from a series of independent AIMD runs. The transparent bars represent the standard deviations within the converged region the AIMD (cf. AIMD statistics). The XC-functionals are distinguished by colors as outlines in the legend.

results, a behaviour often identified, but still heavily debated in experimental research[41]. We do, however, note that the fit is worst for Cu(111) and Ni(111) due to the behaviour discussed in the last paragraph. We discuss a non-linear fit, representing a non-zeroth order desorption behaviour, for Cu(111) in Section IV of the supplementary information. Significant deviation from the zeroth-order result did only appear at coverages below 0.3ML. At coverages above 0.3ML, the deviation from the constant ΔE_{dif} value are well within the error-bars of our AIMD above that coverage and saturate at increasing coverage.

Comparing the three tested XC-functionals, all energetic indicators follow the same order of BEEF-vdW > RPBE-D3 > PBE-D3, with BEEF-vdW binding water more than 0.2eV more strongly than PBE-D3. Based on our simulations, two different factors are at the source of this difference. The first one is the XC-functional quality in describing the interaction of water with the clean metal surface, most easily distinguished by comparing the low coverage adsorption energies. Here a reduction in ΔE_{avg} and ΔE_{int} in the order Au > Cu > Ni > Pt could be observed. The second aspect, relevant at increasing coverages, is the description of water clustering. We will analyze this region in more detail when describing density distribution and hydrogen bond network analysis later on. However, already from the energetic analysis, minima in ΔE_{avg} between 1/2 and 2/3 ML appeared. However, their appearance is not generally observed, where Cu(111) and Ni(111) show clear minima, while they are not observed on Pt(111) and Au(111). Qualitatively this behaviour originates from the formation of a hexagonal surface water layer and the clustering of water at increasing coverages. On Cu(111) surface, this effect is most clear, as shown in 3 e, the minimum located at 0.75ML, 0.5ML and 0.75ML at BEEF-vdW, RPBE-D3, and PBE-D3 functionals, respectively. While beyond these respective coverages, the average adsorption energies are slightly increasing by about 0.05 eV up to 1ML. On Ni(111) ΔE_{avg}-minimum at ca. 0.6 ML appears, being clearly pronounced in the PBE-D3 or RPBE-D3 results (orange and pink bullets in Figure 3 g), while being absent with BEEF-vdW. Both ferromagnetic and non-magnetic Ni(111) have the same results (Figure S9).

The variation in binding sites on stepped surfaces adds complexity to the analysis. We evaluated the comparison on terraces and steps by including the Pt(211) surface in our benchmark, whose adsorption results are shown in figure 3 i-j. To avoid the uncertainty at stepped/terrace sites and to search the global minimum as thorough as possible, four individuals runs from different initial guesses, shown in Figure S5, were applied to run AIMD and

related statistics. Compared to the water/Pt(111) results, water/Pt(211) results have more uncertainty on adsorption energies, especially at the low coverage condition. A thorough analysis of the trajectories applying PBE-D3 and RPBE-D3 showed that the uncertainty of ΔE_{avg} originates from the competition between the adsorption on the undercoordinates step sites and water clustering, which represent two competing local energetic minima of the water adsorption configurations. However, the standard deviation generally lies below 0.1 eV, thus the comparison of XC-functional dependence is influenced marginally. Same as for the (111)-surfaces, the general trend of average adsorption energies is BEEF-vdW > RPBE-D3 > PBE-D3, as shown in Figure 3i.

Several differences between Pt(111) and Pt(211) are worth noting from physical considerations. First, in the low coverage region, compared by Figure 3a and Figure 3i , the water binding on Pt(211) is stronger than Pt(111), as a consequence of the reduced coordination of the step edges. The difference in individual water molecule binding strength at Pt(111) and Pt(211) resulted in 0.15eV in favor of the step edge, with virtually no functional dependence. The second distinct difference appears at intermediate coverages ranging from 0.2ML to 0.7ML, where Pt(211) reaches a saturation of ΔE_{avg} at reduced coverages compared to Pt(111), due to the stronger interaction and better wetting properties at stepped surfaces[42]. Finally, in the high coverage region, from ca. 0.7ML to 1ML ΔE_{avg} increases on Pt(211) while staying constant on Pt(111). This trend is particularly apparent in RPBE-D3 and PBE-D3 results, shown in orange and pink in Figure 3i. A likely explanation for the behaviour in this coverage region the more compact fcc(211) surface in terms of spatial surface area. Thus, a saturated layer of water interacting with the metal is already formed at reduced coverages which blocks the interaction between extra water molecules and metal.

From the slope of integral adsorption energies, compared between Pt(111) and Pt(211), the differential adsorption energies are very close. This result reveals that the water-water interaction still dominates the water adsorption at high coverage on Pt, independent of the specific surface motif.

In addition to the metal and site effect we discussed above, understanding the influence of spin on water adsorption is an elusive question. For decades, research focused on the spin or magnetic effect of water[43], water adsorption[44,45] and water splitting[46]. In our AIMD case, we compared the water adsorption on the ferro- and nonmagnetic Ni(111) surface, as we show in Figure S9 and S20. With the exception of a slightly increased binding strength

up to 0.1eV on ferromagnetic Ni(111) at small coverage, our results show a negligible effect of the metallic spin on the adsorption strength of water.

B. Benchmark results

A direct comparison of our computed and experimentally determined water desorption energetics is shown in Table I. As outlined in the methods section the experimental energetics have been taken from previous reports on TPD, SCAC and TEAS measurements. Here TPD and TEAS probe the activation free energies of desorption, $\Delta G^{\ddagger}_{des}$, while SCAC results probes the enthalpy of desorption ΔH_{des}. The theoretical benchmark of thermodynamic quantities is based on Equation 9 and Equation 10. To better benchmark, results from different experimental methods were refined and listed, while we omitted any references that did not show a clear TPD peak and thus that may cause large uncertainty in an Arrhenius analysis. All energies have been converted onto an eV-scale and we keep the precision consistent with the original experimental results.

For Pt(111) being the most studied surface, all the experimental methods we were able to retrieve data from all three experiment types. TPD and TEAS resulted in comparable $\Delta G^{\ddagger}_{des}$ of 0.54-0.56eV and SCAC, where we collected measurements conducted at the 3 different temperatures, idenitified ΔH_{des} values 0.52-0.56eV. Interestingly, in our benchmark the BEEF-vdW functional fit the values of $\Delta G^{\ddagger}_{des}$ best, resulting in -ΔE_{dif}=0.53eV, while RPBE-D3 performed best when ΔH_{des} was chosen as the benchmark metric with a value of ΔH_{des}=0.58eV.

For Au(111), where we benchmarked against two independent TPD results, we found that the reported $\Delta G^{\ddagger}_{des}$ of 0.43-0.48eV are reproduced remarkable well by the $-\Delta E_{dif}$=0.47eV calculated with BEEF-vdW, while both RPBE-D3 and PBE-D3 overbind. This result is contrasted by the case of Cu(111), where the RPBE-D3 result is most consistent with the TPD result, while BEEF-vdW underbinds.

On Ni(111), the two reported TPD results we collected range between 0.54 and 0.59eV. Although they range within their respective error bars, it leads to the result one experimental result is closer to BEEF-vdW and the other is closer to the RPBE-D3 result. The SCAC result, however, is more consistent with our RPBE-D3 result.

On Pt(211), the TPD results ranging between 0.51 and 0.54 eV aligns best with our

Table I. Tabulated the benchamrk results: water desorption energy at various metal surface from different experimental technique, comparing with the results from AIMD in different XC-functional

Surface	Exp. Technique	Adsorbates	Energy*	Source	BEEF-vdW	RPBE-D3	PBE-D3
			eV		eV	eV	eV
Pt(111)	TPD	D_2O&H_2O	0.539±0.021	[47]	0.53	0.64	0.76
	TPD	H_2O	0.550±0.04	[48]	0.53	0.64	0.76
	TEAS	H_2O	0.561±0.031	[25]	0.53	0.64	0.76
	SCAC(88K)	D_2O,0.5ML	0.564±0.022	[40]	0.44	0.58	0.68
	SCAC(120K)	D_2O,0.5ML	0.532±0.017	[40]	0.44	0.58	0.68
	SCAC(133K)	D_2O,0.5ML	0.52±0.044	[40]	0.44	0.58	0.68
Au(111)	TPD	H_2O	≈ 0.455	[49]	0.47	0.56	0.71
	TPD	H_2O	0.434-0.477	[50]	0.47	0.56	0.71
Cu(111)	TPD	H_2O	≈ 0.572	[51]	0.45	0.56	0.69
Ni(111)	TPD	H_2O	0.539±0.03	[52]	0.50	0.59	0.73
	TPD	H_2O	0.591±0.05	[53]	0.50	0.59	0.73
	SCAC	D_2O,0.5ML	≈ 0.556	[39]	0.41	0.53	0.65
Pt(211)	TPD	H_2O	0.510-0.536	[54]	0.53	0.66	0.79
	TPD	H_2O	0.543±0.01	[42]	0.53	0.66	0.79

* The energy from SCAC technique is the heat of desortpion ΔH_{des}. The energy from TPD and TEAS is the activation free energy of desorption, $\Delta G^{\ddagger}_{des}$.

BEEF-vdW results. Interestingly, the facet of Pt does have little influence on the binding strength both in experiment and theory.

In summary, in most of the cases, BEEF-vdW represents the most reliable XC functional to describe the water adsorption/desorption if benchmarked against TPD and TEAS. For Cu(111) and the SCAC experimental results, on the other hand, the RPBE-D3 results match better. Thus, based on our benchmark, we recommend can recommend both the BEEF-vdW and RPBE-D3 functionals for simulating the water/metal interface, while PBE-D3 always overestimates the water adsorption strength.

C. Water-metal interaction and water-water interaction

From the previous discussion on the water adsorption energies, we highlighted that different exchange correlation functionals have individual features for water adsorption. The energetic difference between BEEF-vdW and PBE-D3 is about 0.2 eV, which is a considerable amount comparing to the water adsorption strength itself. To unravel the origin of the energetic difference among the different functionals, we attempt to separate the interfacial interactions into two parts. The first part is the water-metal interaction, including the physical attraction/repulsion between water molecules and the metal surface. The second part is the water-water interaction at metal surface, including water clustering, hydrogen bond formation and reconstruction.

The surface water density distribution

To visualize the average water distribution, we plotted the density of water, based on both hydrogen and oxygen densities, at the coverages of 1/3 and 2/3 ML, also comparing the results from the three tested XC-functionals and varying metals, as displayed in Figure 4. The full coverage-dependent density plots are shown in Figure S12 and S13.

Generally, water creates a double peak structure in both the H- and O-density close to the metal surfaces, which can be attributed to the formation of a water bilayer, with varying water orientation, facing the surface with H or O, respectively. The respective magnitude of the two peaks varies among the studied surfaces and will be discussed in detail below. In addition to the two distinct peaks, Cu(111) and Ni(111) show extended water tails at intermediate to high coverages, as a consequence of their smaller lattice constant, which leads to a spilling out of water due to compression. Overall comparing the density profiles among the varying metals, based on density peak positions and shape in Figure 4, shows that the water-metal interaction decreases in the order Pt(211)>Ni(111)≈Pt(111)>Cu(111)>Au(111).

The comparison of XC-functionals shows several distinct differences. Overall, the surface water is less ordered with BEEF-vdW, where peaks are broader and further from the surface, RPBE-D3 leads to a more pronounced double peak structure located slightly closer than in the BEEF-vdW. Finally, PBE-D3 shows the strongest ordering of water close to the surface, combined with the lowest distance to the surface.

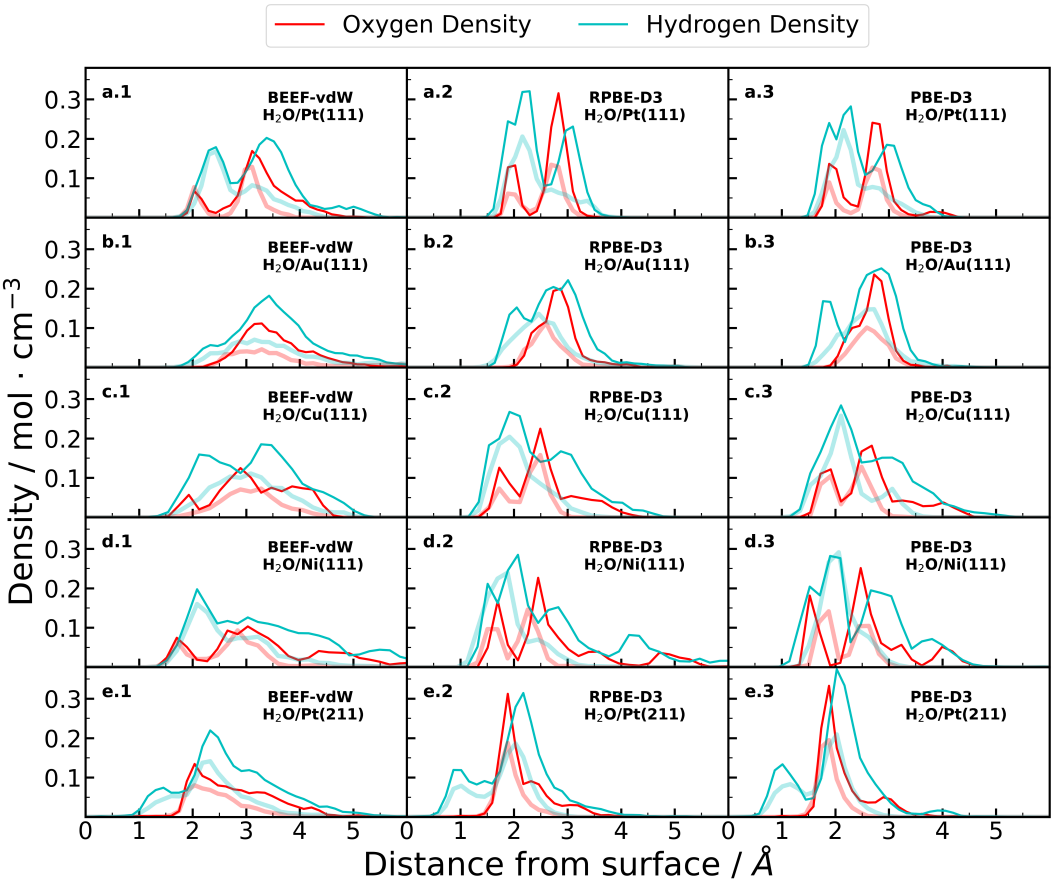

Figure 4. Density distributions of water molecules at Pt(111), Au(111), Cu(111), Ni(111) and Pt(211) comparing from BEEF-vdW (first column), RPBE-D3(second column) and PBE-D3(third column) results. All the density plots are from the AIMD statistics. In each plot, the oxygen density and hydrogen density plot vs. the distance from surface. Oxygen density: in red,hydrogen density: in cyan. The solid plot is at 2/3 ML coverage, the transparent plot is at 1/3 ML coverage. Coverage plots with higher resolution are given in Figure S12 and S13.

Applying BEEF-vdW on Pt(111) resulted in a single hydrogen peak and single broad oxygen peak at very low coverage(< 0.2ML) indicative for the pure physical interaction between water molecules and the surface (see Figure S12 a). Upon increasing beyond 0.25ML, the H- and O-peak (blue and red Figure S12 a, respectively) start splitting into two peaks, and as the coverage increases, these two peaks are growing equally until a coverage of ca. 0.4ML is reached. Beyond 0.4ML, the peak located closer to the Pt(111) surface is

saturated and the second peak keep growing to a broad peak (cf. 1ML plot in Figure S12 a), indicating the water clustering and formation of a bilayer structure.

In contrast to BEEF-vdW, the O-densities show two sharp peaks at 2 and 2.9Å from the metal surface in the RPBE-D3 results, shown in Figure 4 a.2, already at very low coverage, indicating the stronger physical binding between water and the metal, which prevents a widespread water distribution. However, only a single hydrogen peak at 2.2Å keeps growing at low coverages. The near surface O-peaks saturates at 0.4 ML and beyond this coverage the second O-peak starts growing while two H-peaks located at 2.2Å and 3.1Å keep growing equally until ca. 0.8ML, indicating a more tightly bound bilayer structure than with BEEF-vdW. Beyond 0.8 ML, a small third peak starts growing, which indicate the liquid phase water, consistent with previous research, indicating that a 2/3 coverage of water represent an ice-like monolayer[55].

Finally, the PBE-D3 density, in Figure 4 a.3, are comparable to the RPBE-D3 densities but all the peaks are shifted towards the surface at all investigated coverages, reflecting the stronger water-metal interaction than RPBE-D3 results.

The water distribution on Au(111), shown in figure 4 b differs drastically from Pt(111), due to its hydrophobicity[56]. In Figure 4 b.1, the BEEF-vdW results show only one single broad peak of both H- and O- density at 3.5Å. This result indicates that, applying BEEF-vdW, on the Au(111) surface, no clear water bilayer structure forms. This is contrary to the results from RPBE-D3 and PBE-D3 density plots in Figure 4 b.2 and b.3. Here, an obvious H-peak near the Au(111) surface at intermediate coverages from ca. 0.5ML to ca. 0.8 ML, indicative of the creation of bilayer structures under these coverages forms. With the coverage increasing up to 1 ML, these peaks merge into one broad peak again.

The water density above Cu(111), shown in Figure 4 c, behaves like a combination of Pt(111) and Au(111). In Figure 4 c.1, the density plot of water at Cu(111) surface resulting from BEEF-vdW shows a single broad peak at low coverage (transparent line), which splits into multiple peaks at higher coverage (solid line). The single broad peak is comparable to water the density plots for Au(111), shown in panel a. On the other hand, the double peak-feature at intermediate coverages is comparable to Pt(111) one. However, a distinct feature on Cu(111) is the appearance of multiple overlapping density peak in a broad range in the high coverage region, see Figure S12 c, indicating the fierce competition between water-metal and water-water interaction. All three results from different functionals show

the same features, as shown in Figure 4 c.1, c.2 and c.3, while the only difference is the peaks at low coverage are sharper and the first H-peak dominates at all coverage from RPBE-D3 and PBE-D3 results. This results indicates the stronger water-metal interaction at Cu(111) surface from RPBE-D3 and PBE-D3 results, comparing with BEEF-vdW results.

The water distribution on Ni(111), in Figure 4 d, is close to the behaviour on Pt(111) in Figure 4 a, indicating a similar structural evolution of the bilayer formation. At very low coverage(< 0.2ML), a single H-peak and O-peak indicate the pure physical interaction between water molecules and Ni(111). Upon increasing beyond 0.25ML, the H- and O-peaks (in cyan and red in Figure 4 d) start splitting into two peaks, and as the coverage increases, both peaks are growing. After ca. 0.35ML, the first peak is saturated and the second peak keep growing to a broad peak (see full coverage plots in Figure S13 c). The major distinctions between Pt(111) and Ni(111) are the saturation of the first peak at Ni(111) happening already 0.35ML and the overall sharper near-surface density peaks at Ni(111). Especially from the RPBE-D3 and PBE-D3 results, in Figure 4 a.2, a.3 and d.2, d.3, the density peak is higher on Ni(111) than on Pt(111). On the other hand, the overall density distribution at a given coverage is broader on Ni(111) compared to Pt(111) as a consequence of Ni's smaller lattice constant and hence more "crowded" distribution of water molecules on Ni(111). Finally, we address the effect of the spin state of Ni in the Figure S13, where a negligible effect has been identified.

Applying BEEF-vdW on Pt(211) resulted in two distinct hydrogen peaks (in cyan) and a single main oxygen peak(cyan and red in Figure 4 e.1, repectively). All the peaks are located closer to the surface than for the studied fcc(111) surfaces. The most closely located hydrogen peak represents the hydrogen distribution on the step-sites and saturated at ca. 0.5 ML. The second hydrogen peak is the distribution on the other sites or from second layers of stepped sites. Contrarily, the oxygen only forms a single peak is located between the two H-peaks more closely aligned with the second H-peak. This water molecule distribution indicates the molecules orientation is roughly hydrogen down on stepped sites and hydrogen up on other sites. The low coverage behavior is quite different, at ca. 0.1ML, where the hydrogen peak is a small broad peak, indicating that a water molecule is not always specifically adsorbed on stepped sites at low minimal coverages, although we have calculated the difference of adsorption energies, ca. 0.15eV, between Pt(111) sites and Pt(211) sites in Section III A. Results from RPBE-D3 and PBE-D3, shown in Figure 4 e.2 and e.3, are

very similar to the results from BEEF-vdW, except for slightly reduced peak distance to the surface and the sharper density peaks from RPBE-D3 and PBE-D3 results, reflecting the stronger water-metal interaction.

The formation of hydrogen bonds

The formation of hydrogen bonds between waters are critical to the understanding of the water clustering and related water-water and water-metal interactions. Based on the simulated structures from AIMD trajectories, we counted the hydrogen bonds formed in waters, which is shown in Figure 5. On all metal surfaces, the average number of hydrogen bonds increases as the coverage increases up to ca. 0.7 - 0.8 ML. Beyond these coverages the formation of hydrogen bonds saturates likely due to over-saturation of the ice-like water layer on the metal surface. More details are in Figure S11.

Comparing different metal surfaces, the saturated hydrogen bond increases from ca. 1.3 on Au(111) to ca. 1.5 per molecule for Pt(111),Pt(211) and Cu(111), and to ca. 1.75 for Ni(111). The results reveal that the saturated water structures vary at different metal surfaces, which might result from different surface water affinity and lattice constants. On the other hand, the functionals have little impact on the hydrogen bonds on Pt(111) (cf. Figure 5b) but have variations on Au(111) (cf. Figure 5c) and Cu(111) (Figure S11) following the order of PBE-D3≈RPBE-D3 > BEEF-vdW.

Comparing with different sites, in Figure 5 a and b, the average number of hydrogen bond is very close on Pt(111) and Pt(211) surface and the saturated hydrogen bond density is ca. 1.5 per water molecule, which indicate the water-water interaction dominate the bilayer structure at high coverage over different Pt facets. However, at low coverage, the standard deviation of average number of hydrogen bond at Pt(211) is larger than Pt(111), see the error bars in Figure 5 a and b at low coverage, due to the competition between water-water interaction and water adsorption at metal stepped sites.

Considering the hydrogen bond network at metal surface, in Figure 5 d and e, we selected the final structure of AIMD trajectories from BEEF-vdW results at 0.75ML corresponding to the coverage of saturated average number of hydrogen bonds in Figure 5 a. From the top-view configuration panel d, the hexagonal ice layer can be identified on Pt(111) and Au(111), in consistence with previous reports[47,57–59]. For the Cu(111) and Ni(111) surface,

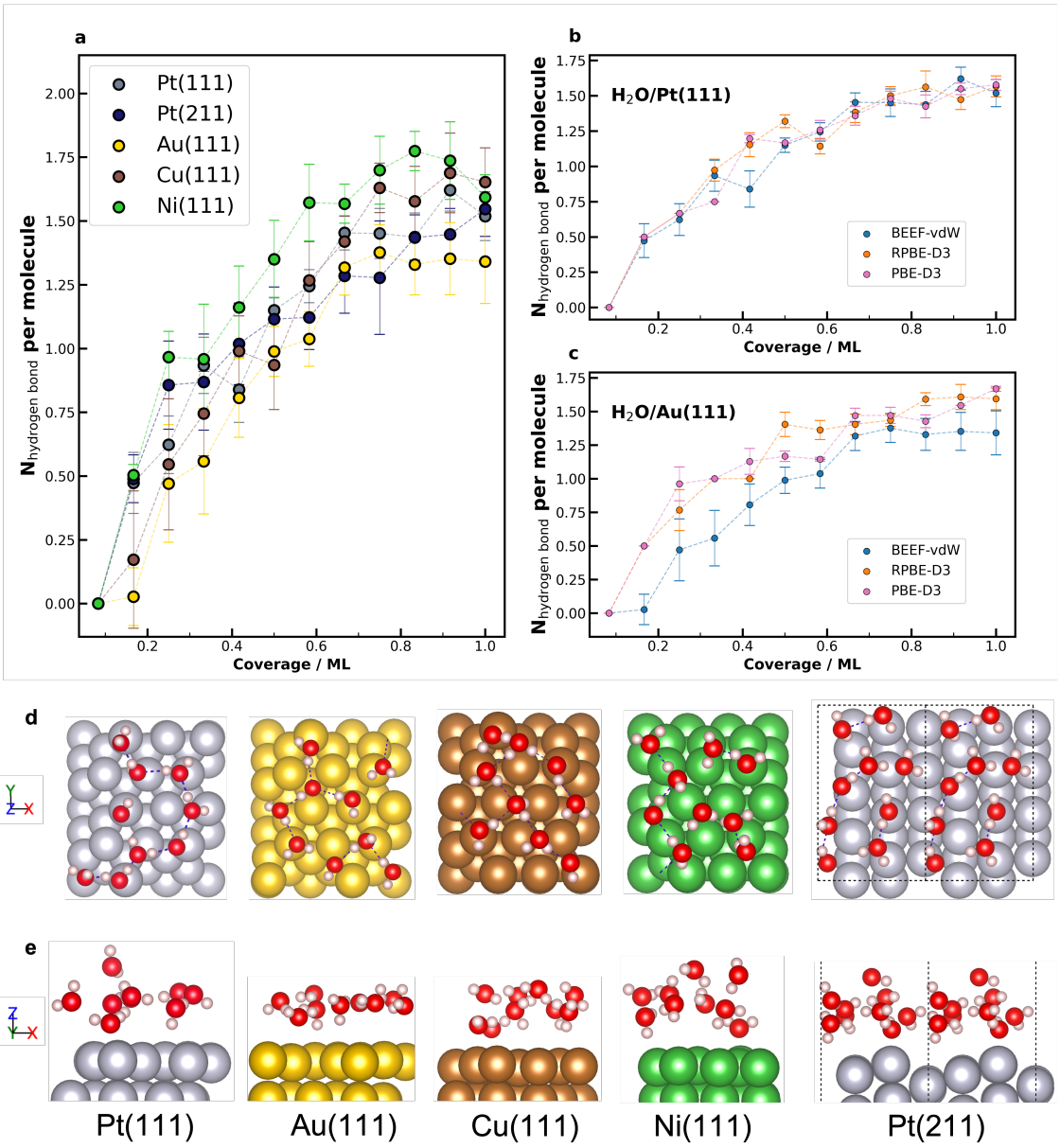

Figure 5. Statistics of the formation of hydrogen bonds. a: The number of hydrogen bond per water molecule at different metal surfaces. Each point shows the average number of hydrogen bond vs. coverage from BEEF-vdW results. The number of hydrogen bond per water molecule using different functionals for b: Pt(111) and c: Au(111). All the hydrogen bonds were counted based on AIMD dataset. The error bars are the standard deviation of the counting. d and e : the top-view and side-view of 0.75ML water at metal surfaces, respectively. From left to right is Pt(111), Au(111), Cu(111), Ni(111), Pt(211) surface. Part of hydrogen bonds were marked in blue dashed line in d.

on the other hand, a twisted hexagonal structure formed[60,61], likely resulting from their. For the stepped Pt(211) surface, the situation is complicated due to the difference in wetting the step and terrace, causes a special linearly shaped water layer on Pt(211)[42,54]. From the side-view of the related structure, in Figure 5 e, for Pt(111), Cu(111) Ni(111) and Pt(211), the bilayer structures can bee seen while the Au(111) surface shows an approximately parallel water layer, due to its weks interaction. The configuration on water distribution along the surface normal is consistent with the density plot in Figure 4.

IV. CONCLUSIONS

Based on our AIMD simulations, we benchmarked the metal-water interactions applying different GGA-level exchange correlation functionals. We found that all investigated XC-functional resulted in a desorption behaviour which justifies a zeroth-order fit, due the early saturation of the adsorption energy at increasing water coverage.

The simulated binding strength of water is functional-dependent following the order BEEF-vdW < RPBE-D3 < PBE-D3. Benchmarking the determined differential water binding energies against experimental TPD, SCAC and TEAS results, we find that that BEEF-vdW is most appropriate to capture the binding strength of water on Pt(111), Pt(211), Ni(111), and Au(111) surfaces. However, RPBE-D3 fits the experimental adsorption energy on the Cu(111) surface the best. Furthermore, RPBE-D3 fits the desorption enthalpy better. PBE-D3 generally overbinds water at the interface with respect to experimental results.

Given the small energetic differences between RPBE-D3 and BEEF-vdW, we conclude that both functionals are capable to capture the metal-water interactions with appropriate accuracy, with RPBE-D3 having the advantage of reduced computational demand.

We find that the binding strength order is reflected by the water density distribution, which varies qualitatively among the compared XC-functionals and metals. On the other hand, the formation of hydrogen bonds between waters varies little among different functionals.

The results of our benchmark offer guidance to reduce systematic errors in future molecular dynamics driven simulations of the solid-water interfaces.

ACKNOWLEDGMENTS

The computational work leading to these results has received funding from the Villum foundation through grants no. 29450 and 9455. The authors acknowledge PRACE for awarding them access to the JUWELS supercomputer at GCS@FZJ in Germany through project 2020235596 and the EuroHPC network for awarding them access the VEGA cluster in Maribor, Slovenia through grant 2020235596. The authors also deeply acknowledge the guidance and mentoring from Prof. Karen Chan in the early stages of the work.

DATA AVAILABILITY STATEMENT

All computational routines and the data shown in this article will be made available at https://github.com/CatTheoryDTU upon acceptance of the article.

REFERENCES

[1]O. Björneholm, M. H. Hansen, A. Hodgson, L.-M. Liu, D. T. Limmer, A. Michaelides, P. Pedevilla, J. Rossmeisl, H. Shen, G. Tocci, E. Tyrode, M.-M. Walz, J. Werner, and H. Bluhm, "Water at interfaces," Chemical Reviews **116**, 7698–7726 (2016), doi: 10.1021/acs.chemrev.6b00045.

[2]S. Gim, K. J. Cho, H.-K. Lim, and H. Kim, "Structure, dynamics, and wettability of water at metal interfaces," Scientific Reports **9**, 14805 (2019).

[3]P. A. Thiel and T. E. Madey, "The interaction of water with solid surfaces: Fundamental aspects," Surface Science Reports **7**, 211–385 (1987).

[4]M. A. Henderson, "The interaction of water with solid surfaces: fundamental aspects revisited," Surface Science Reports **46**, 1–308 (2002).

[5]J.-B. Le and J. Cheng, "Modeling electrochemical interfaces from ab initio molecular dynamics: water adsorption on metal surfaces at potential of zero charge," Current Opinion in Electrochemistry **19**, 129–136 (2020).

[6]J. Carrasco, A. Michaelides, M. Forster, S. Haq, R. Raval, and A. Hodgson, "A one-dimensional ice structure built from pentagons," Nature Materials **8**, 427–431 (2009).

[7]V. Kapil, C. Schran, A. Zen, J. Chen, C. J. Pickard, and A. Michaelides, "The first-principles phase diagram of monolayer nanoconfined water," Nature **609**, 512–516 (2022).

[8]G. A. Kimmel, N. G. Petrik, Z. Dohnálek, and B. D. Kay, "Crystalline ice growth on pt(111) and pd(111): Nonwetting growth on a hydrophobic water monolayer," The Journal of Chemical Physics **126**, 114702 (2007).

[9]M. J. Gillan, D. Alfè, and A. Michaelides, "Perspective: How good is dft for water?" The Journal of Chemical Physics **144**, 130901 (2016), doi: 10.1063/1.4944633.

[10]J. Carrasco, A. Hodgson, and A. Michaelides, "A molecular perspective of water at metal interfaces," Nature Materials **11**, 667–674 (2012).

[11]B. Hammer and J. K. Nørskov, "Theoretical surface science and catalysis—calculations and concepts," in *Advances in Catalysis*, Vol. 45 (Academic Press, 2000) pp. 71–129.

[12]J.-B. Le and J. Cheng, "Modeling electrified metal/water interfaces from ab initio molecular dynamics: Structure and helmholtz capacitance," Current Opinion in Electrochemistry **27**, 100693 (2021).

[13]A. Chen, J.-B. Le, Y. Kuang, and J. Cheng, "Modeling stepped pt/water interfaces at potential of zero charge with ab initio molecular dynamics," The Journal of Chemical Physics **157**, 094702 (2022).

[14]A. Groß and S. Sakong, "Ab initio simulations of water/metal interfaces," Chemical Reviews **122**, 10746–10776 (2022), doi: 10.1021/acs.chemrev.1c00679.

[15]D. T. Limmer, A. P. Willard, P. A. Madden, and D. Chandler, "Water exchange at a hydrated platinum electrode is rare and collective," The Journal of Physical Chemistry C **119**, 24016–24024 (2015), doi: 10.1021/acs.jpcc.5b08137.

[16]B. Hammer, L. B. Hansen, and J. K. Nørskov, "Improved adsorption energetics within density-functional theory using revised perdew-burke-ernzerhof functionals," Physical Review B **59**, 7413–7421 (1999), rPBE.

[17]K. Tonigold and A. Groß, "Dispersive interactions in water bilayers at metallic surfaces: A comparison of the pbe and rpbe functional including semiempirical dispersion corrections," Journal of Computational Chemistry **33**, 695–701 (2012).

[18]S. Sakong, K. Forster-Tonigold, and A. Groß, "The structure of water at a pt(111) electrode and the potential of zero charge studied from first principles," The Journal of Chemical Physics **144**, 194701 (2016).

[19]J. Carrasco, J. Klimeš, and A. Michaelides, "The role of van der waals forces in water adsorption on metals," The Journal of Chemical Physics **138**, 024708 (2013).

[20]I. Hamada, K. Lee, and Y. Morikawa, "Interaction of water with a metal surface: Importance of van der waals forces," Physical Review B **81**, 115452 (2010), pRB.

[21]J. Carrasco, B. Santra, J. Klimeš, and A. Michaelides, "To wet or not to wet? dispersion forces tip the balance for water ice on metals," Physical Review Letters **106**, 026101 (2011), pRL.

[22]J. P. Perdew, K. Burke, and M. Ernzerhof, "Generalized gradient approximation made simple," Physical Review Letters **77**, 3865–3868 (1996), pBE.

[23]A. Groß, "Challenges for ab initio molecular dynamics simulations of electrochemical interfaces," Current Opinion in Electrochemistry **40**, 101345 (2023).

[24]C. T. Campbell and J. R. V. Sellers, "Enthalpies and entropies of adsorption on well-defined oxide surfaces: Experimental measurements," Chemical Reviews **113**, 4106–4135 (2013), doi: 10.1021/cr300329s.

[25]J. L. Daschbach, B. M. Peden, R. S. Smith, and B. D. Kay, "Adsorption, desorption, and clustering of h2o on pt(111)," The Journal of Chemical Physics **120**, 1516–1523 (2004).

[26]V. Rakić and L. Damjanović, "Temperature-programmed desorption (tpd) methods," in *Calorimetry and Thermal Methods in Catalysis*, edited by A. Auroux (Springer Berlin Heidelberg, Berlin, Heidelberg, 2013) pp. 131–174.

[27]J. Kanervo, *Kinetic analysis of temperature-programmed reactions* (Helsinki University of Technology, 2003).

[28]S. Vijay, H. H. Kristoffersen, Y. Katayama, Y. Shao-Horn, I. Chorkendorff, B. Seger, and K. Chan, "How to extract adsorption energies, adsorbate–adsorbate interaction parameters and saturation coverages from temperature programmed desorption experiments," Physical Chemistry Chemical Physics **23**, 24396–24402 (2021).

[29]A. L. Glebov, A. P. Graham, and A. Menzel, "Vibrational spectroscopy of water molecules on pt(111) at submonolayer coverages," Surface Science **427-428**, 22–26 (1999).

[30]C. T. Campbell, "Energies of adsorbed catalytic intermediates on transition metal surfaces: Calorimetric measurements and benchmarks for theory," Accounts of Chemical Research **52**, 984–993 (2019), doi: 10.1021/acs.accounts.8b00579.

[31]G. Kresse and J. Furthmüller, "Efficient iterative schemes for ab initio total-energy calculations using a plane-wave basis set," Physical Review B **54**, 11169–11186 (1996), vASP.

[32]G. Kresse and D. Joubert, "From ultrasoft pseudopotentials to the projector augmented-wave method," Physical Review B **59**, 1758–1775 (1999), pAW.

[33]A. Hjorth Larsen, J. Jørgen Mortensen, J. Blomqvist, I. E. Castelli, R. Christensen, M. Dułak, J. Friis, M. N. Groves, B. Hammer, C. Hargus, E. D. Hermes, P. C. Jennings, P. Bjerre Jensen, J. Kermode, J. R. Kitchin, E. Leonhard Kolsbjerg, J. Kubal, K. Kaasbjerg, S. Lysgaard, J. Bergmann Maronsson, T. Maxson, T. Olsen, L. Pastewka, A. Peterson, C. Rostgaard, J. Schiøtz, O. Schütt, M. Strange, K. S. Thygesen, T. Vegge, L. Vilhelmsen, M. Walter, Z. Zeng, and K. W. Jacobsen, "The atomic simulation environment—a python library for working with atoms," Journal of Physics: Condensed Matter **29**, 273002 (2017), aSE.

[34]H. J. Monkhorst and J. D. Pack, "Special points for brillouin-zone integrations," Physical Review B **13**, 5188–5192 (1976), kPOINTS.

[35]J. Moellmann and S. Grimme, "Dft-d3 study of some molecular crystals," The Journal of Physical Chemistry C **118**, 7615–7621 (2014), dFT-D3.

[36]J. Wellendorff, K. T. Lundgaard, A. Møgelhøj, V. Petzold, D. D. Landis, J. K. Nørskov, T. Bligaard, and K. W. Jacobsen, "Density functionals for surface science: Exchange-correlation model development with bayesian error estimation," Physical Review B **85**, 235149 (2012), bEEF.

[37]M. Dion, H. Rydberg, E. Schröder, D. C. Langreth, and B. I. Lundqvist, "Van der waals density functional for general geometries," Physical Review Letters **92**, 246401 (2004), vdW.

[38]S. Seabold and J. Perktold, "Statsmodels: Econometric and statistical modeling with python," in *Proceedings of the 9th Python in Science Conference*, Vol. 57 (Austin, TX, 2010) pp. 10–25080.

[39]W. Zhao, S. J. Carey, Z. Mao, and C. T. Campbell, "Adsorbed hydroxyl and water on ni(111): Heats of formation by calorimetry," ACS Catalysis **8**, 1485–1489 (2018), doi: 10.1021/acscatal.7b04041.

[40]W. Lew, M. C. Crowe, E. Karp, and C. T. Campbell, "Energy of molecularly adsorbed water on clean pt(111) and pt(111) with coadsorbed oxygen by calorimetry," The Journal of Physical Chemistry C **115**, 9164–9170 (2011), doi: 10.1021/jp201608x.

[41]A. Hodgson and S. Haq, "Water adsorption and the wetting of metal surfaces," Surface Science Reports **64**, 381–451 (2009).

[42]K. Mistry, N. Gerrard, and A. Hodgson, "Wetting of a stepped platinum (211) surface," The Journal of Physical Chemistry C **127**, 4741–4748 (2023), doi:

10.1021/acs.jpcc.2c08360.

[43]Y. Wang, H. Wei, and Z. Li, "Effect of magnetic field on the physical properties of water," Results in Physics **8**, 262–267 (2018).

[44]S. Ozeki, C. Wakai, and S. Ono, "Is a magnetic effect on water adsorption possible?" The Journal of Physical Chemistry **95**, 10557–10559 (1991).

[45]M. E. Grillo, M. W. Finnis, and W. Ranke, "Surface structure and water adsorption on fe_3o_4(111): Spin-density functional theory and on-site coulomb interactions," Physical Review B **77**, 075407 (2008), pRB.

[46]W. Mtangi, V. Kiran, C. Fontanesi, and R. Naaman, "Role of the electron spin polarization in water splitting," The Journal of Physical Chemistry Letters **6**, 4916–4922 (2015), doi: 10.1021/acs.jpclett.5b02419.

[47]S. Haq, J. Harnett, and A. Hodgson, "Growth of thin crystalline ice films on pt(111)," Surface Science **505**, 171–182 (2002).

[48]A. Picolin, C. Busse, A. Redinger, M. Morgenstern, and T. Michely, "Desorption of h2o from flat and stepped pt(111)," The Journal of Physical Chemistry C **113**, 691–697 (2009).

[49]B. D. Kay, K. R. Lykke, J. R. Creighton, and S. J. Ward, "The influence of adsorbate–absorbate hydrogen bonding in molecular chemisorption: Nh3, hf, and h2o on au(111)," The Journal of Chemical Physics **91**, 5120–5121 (1989).

[50]M. A. Lazaga, D. T. Wickham, D. H. Parker, G. N. Kastanas, and B. E. Koel, "Reactivity of oxygen adatoms on the au(111) surface," in *Catalytic Selective Oxidation*, ACS Symposium Series, Vol. 523 (American Chemical Society, 1993) Book section 8, pp. 90–109, doi:10.1021/bk-1993-0523.ch008.

[51]B. J. Hinch and L. H. Dubois, "Stable and metastable phases of water adsorbed on cu(111)," The Journal of Chemical Physics **96**, 3262–3268 (1992).

[52]M. Schulze, R. Reißner, K. Bolwin, and W. Kuch, "Interaction of water with clean and oxygen precovered nickel surfaces," Fresenius' Journal of Analytical Chemistry **353**, 661–665 (1995).

[53]T. Pache, H. P. Steinrück, W. Huber, and D. Menzel, "The adsorption of h2o on clean and oxygen precovered ni(111) studied by arups and tpd," Surface Science **224**, 195–214 (1989).

[54]C. Badan, M. T. M. Koper, and L. B. F. Juurlink, "How well does pt(211) represent pt[n(111) × (100)] surfaces in adsorption/desorption?" The Journal of Physical Chemistry

C **119**, 13551–13560 (2015).

[55]H. H. Heenen, J. A. Gauthier, H. H. Kristoffersen, T. Ludwig, and K. Chan, "Solvation at metal/water interfaces: An ab initio molecular dynamics benchmark of common computational approaches," The Journal of Chemical Physics **152**, 144703 (2020).

[56]V. Wieser, P. Bilotto, U. Ramach, H. Yuan, K. Schwenzfeier, H.-W. Cheng, and M. Valtiner, "Novel in situ sensing surface forces apparatus for measuring gold versus gold, hydrophobic, and biophysical interactions," Journal of Vacuum Science & Technology A **39** (2021), 10.1116/6.0000611.

[57]T. Lankau and I. L. Cooper, "(h2o)6 on a virtual metal surface: testing the surface ice rules," The Journal of Physical Chemistry A **105**, 4084–4095 (2001), doi: 10.1021/jp0035986.

[58]T. Sugimoto and Y. Matsumoto, "Orientational ordering in heteroepitaxial water ice on metal surfaces," Physical Chemistry Chemical Physics **22**, 16453–16466 (2020).

[59]R. Ma, D. Cao, C. Zhu, Y. Tian, J. Peng, J. Guo, J. Chen, X.-Z. Li, J. S. Francisco, X. C. Zeng, L.-M. Xu, E.-G. Wang, and Y. Jiang, "Atomic imaging of the edge structure and growth of a two-dimensional hexagonal ice," Nature **577**, 60–63 (2020).

[60]S. Duan, I. Y. Zhang, Z. Xie, and X. Xu, "Identification of water hexamer on cu(111) surfaces," Journal of the American Chemical Society **142**, 6902–6906 (2020), doi: 10.1021/jacs.0c01549.

[61]M. Nakamura and M. Ito, "Ring hexamer like cluster molecules of water formed on a ni(111) surface," Chemical Physics Letters **384**, 256–261 (2004).